

# Tracking Extended Quintessence

Carlo Baccigalupi<sup>1\*</sup>, Sabino Matarrese<sup>2,3†</sup>, Francesca Perrotta<sup>1‡</sup>

<sup>1</sup> SISSA/ISAS, Via Beirut 4, 34014 Trieste, Italy;

<sup>2</sup> Dipartimento di Fisica ‘Galileo Galilei’, Università di Padova,

and INFN, Sezione di Padova, Via Marzolo 8, 35131 Padova, Italy;

<sup>3</sup> Max-Planck-Institut für Astrophysik, Karl-Schwarzschild-Strasse 1, D-85748 Garching, Germany.

We investigate the cosmological role of a Tracking Field  $\phi$  in Extended Quintessence scenarios, where the dynamical vacuum energy driving the acceleration of the universe today possesses an explicit coupling with the Ricci scalar,  $R$ , of the form  $F(\phi)R/2$ , where  $F(\phi)$  mimics General Relativity today,  $F(\phi_0) = 1/8\pi G$ . We analyse explicit non-minimally coupled (NMC) models where  $F(\phi) = 1/8\pi G + \xi(\phi^2 - \phi_0^2)$ , with  $\xi$  is the coupling constant and  $\phi_0$  is the Q value today. Tracker solutions for these NMC models, with inverse power-law potentials, possess an initial enhancement of the scalar field dynamics, named *R*-boost, caused by the effective potential generated by the Ricci scalar in the Klein-Gordon equation. During this phase the field performs a “gravitational” slow rolling until the true potential becomes important. We give accurate analytic formulas describing the *R*-boost, showing that the Quintessence energy in this phase scales with the redshift  $z$  as  $(1+z)^2$ . When the *R*-boost ends, the field trajectory matches the tracker solution in minimally coupled theories. We compute perturbations in these Tracking Extended Quintessence models, by integrating the full set of equations for the evolution of linear fluctuations in scalar-tensor theories of gravity, and assuming Gaussian scale-invariant initial perturbations. The Integrated Sachs Wolfe (ISW) effect on the Cosmic Microwave Background (CMB) angular spectrum causes a change  $\delta C_\ell/C_\ell \simeq 2[1 - 8\pi GF(\phi_{dec})]$  at  $\ell \lesssim 10$ , where  $dec$  stands for decoupling. Similarly, the CMB acoustic peaks multipoles shift compared to ordinary tracking Quintessence models by roughly an amount  $\delta\ell/\ell \simeq [8\pi GF(\phi_{dec}) - 1]/8$ . The turnover wavenumber  $k_{turn}$  in the matter power spectrum shifts by an amount  $\delta k_{turn}/k_{turn} \simeq [1 - 8\pi GF(\phi_{eq})]/2$ , where  $eq$  stands for matter-radiation equivalence. All these corrections may assume positive as well as negative values, depending on the sign of the NMC parameter  $\xi$ . We show that the above effects can be as large as 10 – 30% with respect to equivalent cosmological constant and ordinary tracking Quintessence models, respecting all the existing experimental constraints on scalar-tensor theories of gravity. These results demonstrate that the playground where the next decade data will have their impact includes the nature of the dark energy in the Universe, as well as the structure of the theory of gravity.

## I. INTRODUCTION

Following the experimental evidence in favor of an accelerating universe [1–3], the cosmological role of a minimally-coupled scalar field, considered as a “Quintessence” component (which we call here Q or  $\phi$ , equivalently), providing the dominant contribution to the energy density of the Universe today in the form of dynamical vacuum energy, has been widely analyzed in the recent past [4] - [10]. The main feature of this dynamical vacuum energy component, that could also allow to distinguish it from a cosmological constant, is its time-dependence and the wide range of possibilities for its equation of state. Moreover, by the principle of general covariance this time varying scalar field should also develop spatial perturbations.

In a number of recent papers the available range of couplings between Q and other physical components has been explored. The possible coupling between a Quintessence field and light matter fields has been investigated in [11] and is subject to restrictions coming from the observational constraints on the time variation of the constants of nature. Also, some recent work explores the cosmological consequences of a coupling between Quintessence and matter fields [12]. The possible coupling between Q and the Ricci scalar  $R$  was the subject of our recent analysis [13], where the observable impact of such a coupling has been thoroughly investigated. Within this ‘Extended Quintessence’ (EQ) model two sets of theories were studied: Induced Gravity (IG, originally proposed in [14]) and Non-Minimal Coupling (NMC, see [15] for an extensive overview). In both models the term describing the coupling between the Ricci scalar  $R$  and the Quintessence field  $\phi$  in the Lagrangian has the form  $F(\phi)R/2$ , where  $F(\phi) = \xi\phi^2$ ; the difference between the two models is that in the NMC model the Lagrangian contains also the ordinary gravitational term  $R/16\pi G$ , that is instead absent in IG. Both models belong to the general class of scalar-tensor theories of gravity. The effects on

---

\*bacci@sissa.it

†matarrese@pd.infn.it

‡perrotta@sissa.it

Cosmic Microwave Background (CMB) anisotropies, as well as on Large Scale Structure (LSS), have been described and numerically computed for several values of  $\xi > 0$ ; they turned out to be similar for IG and NMC, although for different values of the coupling constant. The main results of our previous study were a modification of the low redshift dynamics, enhancing the Integrated Sachs Wolfe effect (ISW), as well as a shift of the CMB acoustic peaks and matter power spectrum turnover because of the dynamics of the Hubble length. Predicting in detail the shape and the position of the acoustic peaks in a given cosmological model is of course important in view of the formidable observations of the next decade [16], but it is also of great importance at present, because of the strong evidence in favor of the existence of subdegree acoustic oscillations in the latest CMB data [17,18].

As detailed in our previous paper [13], we named our models ‘Extended Quintessence’, in analogy with the ‘extended inflation’ models [19], proposed in the late eighties to rescue the original idea of inflation based on a first-order phase transition. In those models a Jordan-Brans-Dicke (JBD) scalar field [20] was added to the action to solve the ‘graceful exit’ problem of ‘old inflation’. The idea of using a non-minimally coupled scalar field as a decaying cosmological constant dates back to a paper by Dolgov [21] in 1983, which however radically differs from the present class of models by the absence of a true potential energy for the scalar field. The background dynamical properties of a Quintessence field coupled to the Ricci curvature have also been recently studied in [22], [23] and [24], [25] where, in particular, the existence and stability of cosmological scaling solutions was analyzed. Models in scalar-tensor theories of gravity involving scalar matter couplings have also been studied [26].

Let us come now to the subject of the present work. The existence of a considerable amount of vacuum energy in the Universe, as observations seem to imply, brings together two conceptual problems. The first is the so-called “coincidence” problem, namely the fact that we are right now in the phase in which the vacuum energy is starting to dominate over matter. The second is a “fine-tuning” problem, which arises merely from the fact that if the vacuum energy is constant, like in the ‘standard’ cosmological constant scenario, then, at the beginning of the radiation era the  $Q$  energy density should have been vanishingly small compared with both radiation and matter.

Important recent work demonstrated that the Quintessence scenario can avoid such fine tunings, while a cosmological constant fitting the data would be affected by both problems. Indeed, in the Quintessence scenario one can select a subclass of models which admit “tracking solutions” [9]: following early work by Ratra and Peebles [7], it was shown how the observed amount of scalar field energy density today can be reached starting from a very wide set of initial conditions, covering tens of orders of magnitude. In particular, the Quintessence could have been initially at the level of the ordinary matter, thus being likely one of the products of the decay of the vacuum energy responsible for the inflation era.

Here we face the extension of tracking phenomenology in EQ; we find important results, both for background dynamics and perturbations, and we name this scenario Tracking Extended Quintessence (TEQ). We consider a NMC model for the coupling between  $Q$  and  $R$ . We first analyse the background evolution, accurately studying the Quintessence dynamics in the radiation dominated (RDE) and matter dominated (MDE) eras. Then, we compute the evolution of cosmological perturbations pointing out important observable effects on CMB and LSS.

The work is organized as follows: in Sec. II we recall the relevant equations, and we refer to previous works [13,10] for a complete presentation of the dynamical system for the background and for the perturbations in non-minimally coupled scalar field cosmologies; Sec. III contains the analysis of tracking solutions; Secs. IV and V contain the description and a discussion of the effects on CMB and LSS, respectively; Sec. VI discusses how these effects change if we vary the form of the  $Q$ -field potential. Finally, Sec. VII contains a summary of our results and some concluding remarks.

## II. COSMOLOGY IN SCALAR-TENSOR THEORIES OF GRAVITY

In this Section we review the relevant equations in scalar-tensor theories of gravity, for the background evolution and linear perturbations. For more details, we refer to previous works [13,10].

Following [27], scalar-tensor theories of gravity are represented by the action

$$S = \int d^4x \sqrt{-g} \left[ \frac{1}{2}f(\phi, R) - \frac{1}{2}\omega(\phi)\phi^{;\mu}\phi_{;\mu} - V(\phi) + L_{fluid} \right], \quad (1)$$

where  $R$  is the Ricci scalar, and  $L_{fluid}$  includes all components except for  $\phi$ , that we suppose coupled only with gravity.

The models for  $f(\phi, R)$  that we investigate here are simply a product of a function of  $\phi$  and  $R$ ; also we assume a standard form for the kinetic part:

$$f(\phi, R) = F(\phi)R, \quad \omega(\phi) = 1. \quad (2)$$

As in [13], we assume the cosmological metric has the flat Friedmann-Robertson-Walker (FRW) form:

$$ds^2 = a^2[-d\tau^2 + (\delta_{ij} + h_{ij})dx^i dx^j], \quad (3)$$

where  $a(\tau)$  is the scale factor,  $\tau$  is the conformal time and  $h_{ij}$  represents the perturbations in the synchronous gauge, to be discussed later. Our units are  $c \equiv 1$ , and we adopt the signature  $(-, +, +, +)$ .

In the next subsections we describe the evolution equations for the relevant quantities, for the background and linear perturbations.

### A. Background

The background FRW equations read

$$\mathcal{H}^2 = \left( \frac{\dot{a}}{a} \right)^2 = \frac{1}{3F} \left( a^2 \rho_{fluid} + \frac{1}{2} \dot{\phi}^2 + a^2 V - 3\mathcal{H}\dot{F} \right) , \quad (4)$$

$$\dot{\mathcal{H}} = \mathcal{H}^2 - \frac{1}{2F} \left( a^2 (\rho_{fluid} + p_{fluid}) + \dot{\phi}^2 + \ddot{F} - 2\mathcal{H}\dot{F} \right) , \quad (5)$$

where the dot denotes differentiation with respect to the conformal time  $\tau$ ; note that in our framework  $1/F$  today must be  $8\pi G$ .

The Klein-Gordon equation reads

$$\ddot{\phi} + 2\mathcal{H}\dot{\phi} = \frac{a^2}{2} F_\phi R - a^2 V_\phi , \quad (6)$$

where the subscript  $\phi$  denotes differentiation w.r.t.  $\phi$ . Furthermore, the continuity equations for the individual fluid components are not directly affected by the changes in the gravitational field equation, and for the  $i$ -th component we have

$$\dot{\rho}_i = -3\mathcal{H}(\rho_i + p_i) . \quad (7)$$

Let us give now useful expressions for the Ricci scalar in scalar-tensor theories:

$$R = -\frac{1}{F} \left[ -\rho_{fluid} + 3p_{fluid} + \frac{\dot{\phi}^2}{a^2} - 4V + 3 \left( \frac{\ddot{F}}{a^2} + 2\frac{\mathcal{H}\dot{F}}{a^2} \right) \right] . \quad (8)$$

Another expression that will be useful in the following is

$$R = \frac{6}{a^2} (\dot{\mathcal{H}}^2 + \mathcal{H}^2) . \quad (9)$$

As discussed in more detail in [13], let us recall the two experimental constraints that these models have to satisfy. One comes from the time variation of the gravitational constant in scalar-tensor gravity theories,

$$\left| \frac{G_t}{G} \right| = -\frac{F_t}{F} , \quad (10)$$

where the subscript  $t$  denotes differentiation w.r.t. the cosmic time  $t$ ;  $G_t/G$  is bounded by local laboratory and solar system experiments [28] to be

$$\frac{G_t}{G} \leq 10^{-11} \text{ per year} . \quad (11)$$

Another independent experimental constraint comes from the effects induced on photon trajectories [29]:

$$\omega_{JBD} \equiv \frac{F_0}{F_{\phi 0}^2} \geq 500 , \quad (12)$$

where  $F_{\phi 0}$  is the derivative of  $F$  w.r.t.  $\phi$  calculated at the present time. The latter bound does not depend on the particular cosmological trajectory at hand, since in contrast to (11), it does not involve time derivatives, but only the present value of the field.

Let us define now the form of  $F(\phi)$  that we consider here. We analyse non-minimally coupled scalar field models, defined as in [13]. The term multiplying the curvature scalar  $R$  is made of a dominant contribution, which is a constant, plus one depending on  $\phi$ :

$$F(\phi) \equiv \frac{1}{8\pi G} + \tilde{F}(\phi) - \tilde{F}(\phi_0) , \quad (13)$$

where

$$\tilde{F}(\phi) = \xi\phi^2 . \quad (14)$$

The second constraint (12) turns out to be the dominant one for our models; as is very easy to verify, it gives rise to the following condition:

$$\xi \lesssim \frac{10^{-2}}{2\sqrt{G}\phi_0} . \quad (15)$$

The only remaining quantity to specify in our model is the potential for the field  $\phi$ , responsible for the dominant part of the vacuum energy today. We adopt here inverse power-law potentials, as originally suggested by Ratra and Peebles [7], and found in some phenomenological supersymmetry breaking models [9,30], although cosine [6] and exponential [5] potentials have also been proposed in the literature. We take

$$V(\phi) = \frac{M^{4+\alpha}}{\phi^\alpha} , \quad (16)$$

where the value of  $\alpha > 0$  will be specified later and the mass-scale  $M$  is fixed by the level of energy contribution today from the Quintessence.

Let us conclude this subsection by defining the quantities describing the Q energy density and pressure. By considering the kinetic and potential terms, we generalize in a straightforward way the definitions in ordinary General Relativity:

$$\rho_\phi = \frac{1}{2a^2}\dot{\phi}^2 + V(\phi) . \quad (17)$$

Similarly, the Quintessence pressure assumes the form

$$p_\phi = \frac{1}{2a^2}\dot{\phi}^2 - V(\phi) . \quad (18)$$

However, as it is evident from equation (4), there are other terms in the right-hand side that could be included into the Q energy density and pressure, coming directly from the coupling with  $R$ . Thus we define here the generalized Q energy density and pressure, that include all the NMC terms:

$$\tilde{\rho}_\phi = \frac{1}{2a^2}\dot{\phi}^2 + V(\phi) - \frac{3\mathcal{H}\dot{F}}{a^2} . \quad (19)$$

$$\tilde{p}_\phi = \frac{1}{2a^2}\dot{\phi}^2 - V(\phi) + \frac{\ddot{F}}{a^2} + \frac{\mathcal{H}\dot{F}}{a^2} . \quad (20)$$

In the next Section we will see how  $\rho_\phi, p_\phi$  may differ substantially from  $\tilde{\rho}_\phi, \tilde{p}_\phi$ , while in general they become nearly identical in the MDE.

## B. Perturbations

As in [13,10], we adopt here the treatment of the perturbations based on the formalism developed in [27] to describe the evolution of perturbations in the synchronous gauge. The perturbing tensor in Eq.(3) is Fourier transformed and the generic component at wavevector  $\mathbf{k}$  may be written as

$$h_{ij}(\mathbf{k}, \tau) = \hat{\mathbf{k}}_i \hat{\mathbf{k}}_j h(\mathbf{k}, \tau) + (\hat{\mathbf{k}}_i \hat{\mathbf{k}}_j - \frac{1}{3}\delta_{ij})6\eta(\mathbf{k}, \tau) , \quad (21)$$

where  $h$  denotes the trace of  $h_{ij}$  and  $\eta$  represents the traceless component; we omit the arguments  $(\mathbf{k}, \tau)$  in the following.

The perturbed Einstein equations read

$$k^2\eta - \frac{1}{2}\mathcal{H}\dot{h} = -\frac{a^2\delta\rho}{2}, \quad (22)$$

$$k^2\dot{\eta} = \frac{a^2(p + \rho)\theta}{2}, \quad (23)$$

$$\ddot{h} + 2\mathcal{H}\dot{h} - 2k^2\eta = -3a^2\delta p, \quad (24)$$

$$\ddot{h} + 6\ddot{\eta} + 2\mathcal{H}(\dot{h} + 6\dot{\eta}) - 2k^2\eta = -3a^2(p + \rho)\sigma. \quad (25)$$

The perturbed density, pressure and velocity in the synchronous gauge assume the form

$$\delta\rho = \frac{1}{F} \left[ \delta\rho_{fluid} + \frac{\dot{\phi}\delta\dot{\phi}}{a^2} + \frac{1}{2}(-F_\phi R + 2V_\phi)\delta\phi - 3\frac{\mathcal{H}\delta\dot{F}}{a^2} - \left(\frac{\rho + 3p}{2} + \frac{k^2}{a^2}\right)\delta F + \frac{\dot{F}\dot{h}}{6a^2} \right], \quad (26)$$

$$\delta p = \frac{1}{F} \left[ \delta p_{fluid} + \frac{\dot{\phi}\delta\dot{\phi}}{a^2} + \frac{1}{2}(F_\phi R - 2V_\phi)\delta\phi + \frac{\delta\ddot{F}}{a^2} + \frac{\mathcal{H}\delta\dot{F}}{a^2} + \left(\frac{p - \rho}{2} + \frac{2k^2}{3a^2}\right)\delta F - \frac{1}{9}\frac{\dot{F}\dot{h}}{a^2} \right], \quad (27)$$

$$(p + \rho)\theta = \frac{(p_{fluid} + \rho_{fluid})\theta_{fluid}}{F} - \frac{k^2}{a^2} \left( \frac{-\dot{\phi}\delta\phi - \delta\dot{F} + \mathcal{H}\delta F}{F} \right), \quad (28)$$

$$(p + \rho)\sigma = \frac{(p_{fluid} + \rho_{fluid})\sigma_{fluid}}{F} + \frac{2k^2}{3a^2F} \left( \delta F + 3\frac{\dot{F}}{k^2}(\dot{\eta} + \frac{\dot{h}}{6}) \right), \quad (29)$$

where everything labeled with *fluid* has the form as in ordinary General Relativity, and obeys the perturbed continuity equations [10]. There remains the perturbed Klein-Gordon equation:

$$\delta\ddot{\phi} + 2\mathcal{H}\delta\dot{\phi} + \left[ k^2 + a^2 \left( \frac{-F_\phi R + 2V_\phi}{2} \right)_\phi \right] \delta\phi = \frac{\dot{\phi}\dot{h}}{6} + \frac{a^2}{2}F_\phi\delta R. \quad (30)$$

Note the presence of the Ricci curvature scalar  $R$  in the left-hand side, as well as its perturbation  $\delta R$  in the right-hand side: the latter term is not trivial, since it contains  $\delta\ddot{\phi}$ ; from [27] we see that in the synchronous gauge it is in fact

$$\delta R = \frac{1}{3a^2} \left( \ddot{h} - 3\mathcal{H}\dot{h} + 2k^2\eta \right), \quad (31)$$

so that the Klein Gordon equation, using Eq.(24), assumes the complicated form below:

$$\begin{aligned} \delta\ddot{\phi} \left( 1 - \frac{1}{2} \frac{F_\phi^2}{F} \right) + \left[ 2\mathcal{H} - \frac{F_\phi}{2F} \left( \dot{\phi} + 2F_{\phi\phi}\dot{\phi} + \mathcal{H}F_\phi \right) \right] \delta\dot{\phi} + \\ + \left[ k^2 + a^2 \left( \frac{-F_\phi R + 2V_\phi}{2} \right)_\phi - \frac{F_\phi}{2F} \left( \frac{1}{2}a^2F_\phi R - a^2V_\phi + F_{\phi\phi\phi}\dot{\phi}^2 + F_{\phi\phi}\ddot{\phi} + \mathcal{H}F_{\phi\phi}\ddot{\phi} \right) \right] \delta\phi + \\ + F_\phi \left( \frac{a^2p - a^2\rho}{2} + \frac{2}{3}k^2 \right) \delta\phi = \\ = \frac{\dot{\phi}\dot{h}}{6} - \frac{F_\phi}{6} \left( \mathcal{H}\dot{h} - 10k^2\eta \right) + \frac{F_\phi}{2F}a^2\delta p_{fluid} - \frac{F_\phi^2}{18F}\dot{\phi}\dot{h}. \end{aligned} \quad (32)$$

This set of differential equations can be integrated once initial conditions on the metric and fluid perturbations are given; in this work we adopt adiabatic initial conditions for the various components as well as Gaussian and scale-invariant initial perturbations (see [13,10]).

### III. TRACKING EXTENDED QUINTESSENCE

Let us now turn to the study of tracking solutions in our model. As we already mentioned in the Introduction, the existence of this kind of trajectories was first pointed out by Ratra and Peebles [7]. In [9], it was realized that they could be used to solve one of the two problems existing in Quintessence scenarios, namely the fine-tuning on the initial conditions; this is in favor of Quintessence compared with the ordinary cosmological constant models, which is affected by both the coincidence and fine tuning problems.

For what concerns the background parameters, we require the present closure density of Quintessence to be  $\Omega_\phi = 0.7$ , with Cold Dark Matter at  $\Omega_{CDM} = 0.253$ , three families of massless neutrinos, baryon content  $\Omega_b = 0.047$  and Hubble constant  $H_0 = 100h_{100}$  Km/sec/Mpc (or  $h_{100} = 0.65$  thus keeping  $\Omega_b h_{100}^2 = 0.020$ ). In section V we will explore the dependence of our results on the potential index  $\alpha$ . Here we adopt  $\alpha = 2$ . The case  $\alpha = 1$  was studied in [13], where however, we did not explore the properties of tracking solutions. As we will discuss in Section VI, however, the dynamical relevance of tracking solutions, becomes more and more relevant, as the potential slope increases, so, our main results of [13] are not essentially modified.

In Figure 1 we plot the evolution of the energy density of the cosmic fluid components (radiation, matter and Quintessence) as a function of redshift, in several models that we are going to describe now. The plotted curves are  $\rho_r$ ,  $\rho_m$  and  $\rho_\phi$ . The high, dotted lines represent radiation and matter, which do possess the well known scalings  $\rho_r \sim 1/a^4$ ,  $\rho_m \sim 1/a^3$ . Equivalence occurs roughly at  $1+z_{eq} \simeq 5 \times 10^3$ . The other curves represent tracker solutions for the Quintessence energy density  $\rho_\phi$ . We will describe in detail each curve in the next subsections; let us give here some general considerations. For each curve, the constant  $M$  in Eq.(16) has been chosen to produce the required  $\Omega_\phi$  today. The NMC dimensionless coupling constant is taken as

$$|\xi| = 1.5 \times 10^{-2}, \quad (33)$$

so as to satisfy the experimental constraints (12), because in all the cases shown in Fig.1 the present value of  $\phi$  is  $\phi_0 \simeq 0.35 M_P$ , where  $M_P = 1/\sqrt{G}$ . Also we study both positive and negative values of  $\xi$ .  $\phi_0$  is reached starting from initial conditions  $\phi_{beg} \ll \phi_0$  and  $\dot{\phi}_{beg}$  which can vary by several tens of orders of magnitude thanks to the capability of tracker solutions to remove any fine tuning of the initial conditions. In fact, it can be immediately noted from the curves in Fig.1 that, despite the huge range of initial values of the energy density, the Q component is going to dominate today at the chosen level. The final aspect we wish to point out before going to a detailed analysis of the dynamics in MDE and RDE, is that we plotted  $\rho_\phi$  in the figure, which is always positive, as it is evident from its definition (17). This is not true for  $\tilde{\rho}_\phi$  defined in (19), because the NMC terms may be negative, and in fact they overcome the kinetic and potential energy, as we will see below; this feature was first found and discussed in [13].

#### A. TEQ-trajectories in the Radiation Dominated Era: *R*-boost

To understand what happens, let us study the Klein-Gordon equation during the Radiation Dominated Era (RDE). The first feature to note is the behavior of the Ricci scalar  $R$ . The dominant fluid is radiation, so that  $a \sim \tau$ , and this could yield the wrong idea that  $R = 0$  from Eq.(9). Actually this is not true as it is evident from Eq.(8): the first two terms  $\rho_{fluid} - 3p_{fluid}$  take zero contribution from radiation, but there is a residual contribution  $\rho_m$ , from the subdominant matter component. Thus, there is a divergence  $R \propto 1/a^3$  as  $a \rightarrow 0$ . Also, we will see in a moment that the other terms in Eq.(8), as well as the little dynamics implied by the overall factor  $1/F$  do not change this argument; in conclusion the behavior of  $R$  in the RDE is

$$R \simeq \frac{8\pi G \rho_{m0}}{a^3} = \frac{3H_0^2(\Omega_{CDM} + \Omega_b)}{a^3} \quad \text{for } a \rightarrow 0. \quad (34)$$

This implies that on the RHS of the Klein Gordon equation (6) the term multiplying  $R$  diverges as  $1/a$  and has the same sign of  $\xi$  since  $\phi$  is assumed to be always positive. This generates a “gravitational” effective potential causing an enhancement of the dynamics of  $\phi$  at early times, that we name “*R*-boost”. The field accelerates until the friction term  $2\mathcal{H}\dot{\phi}$  reaches a value that is comparable to the *R*-boost term on the RHS. After that, Q enters a phase of slow roll driven by the friction and the *R*-boost terms only:

$$2\mathcal{H}\dot{\phi} \simeq \frac{a^2 RF_\phi}{2}. \quad (35)$$

The slow roll holds until the true potential energy from  $V$  becomes important in the Klein Gordon equation. This dynamics is manifest in Fig.2, where the absolute values of the four terms in the Klein Gordon equation are plotted. The thin solid line is the potential term, that is subdominant until  $1+z \lesssim 1000$ . The heavy dashed line is the friction

term and the solid heavy one is the  $R$ -boost term. In a very short time the friction grows from zero (the initial  $Q$  velocity is here taken to be zero) until it reaches the  $R$ -boost term, setting the onset of the slow rolling regime. The thin dashed line is the  $Q$  acceleration,  $\ddot{\phi}$ , which is positive and decreasing initially; then, it becomes negative (deceleration) at the cusp corresponding to  $1+z \sim 10^7$ , and again positive at  $1+z \sim 10^3$  when the potential energy becomes important and the tracker behavior in the MDE starts.

It is quite simple to write an accurate analytic form for the solution during the  $R$ -boost. By using Eqs.(34,35), and the behavior of  $a$  in the RDE,  $a \simeq \sqrt{8\pi G \rho_r^0/3} \cdot \tau$ , we easily get

$$\phi = \phi_{beg} \exp [\mathcal{C}(\tau - \tau_{beg})] , \quad (36)$$

where

$$\mathcal{C} = \frac{3H_0^2(\Omega_{CDM} + \Omega_b)}{2\sqrt{8\pi G \rho_r^0/3}} \xi . \quad (37)$$

With our choice of parameters,  $\mathcal{C} \simeq 7 \cdot 10^{-3} \xi \text{ Mpc}^{-1}$ , which implies that the exponent in (36) remains much smaller than one at all relevant times. Therefore,

$$\phi \simeq \phi_{beg} [1 + \mathcal{C}(\tau - \tau_{beg})] . \quad (38)$$

The behavior expressed by Eqs.(36, 38) corresponds to the dotted dashed line in Fig.1, which mimics very tightly the  $R$ -boost solution. Indeed in this phase the  $Q$  kinetic energy density dominates and Eq.(38) implies

$$\frac{1}{2}\dot{\phi}_t^2 = \frac{1}{2}\frac{\dot{\phi}}{a^2} = \frac{1}{2}\frac{\phi_{beg}^2 \mathcal{C}^2}{a^2} . \quad (39)$$

The dot-dashed line in Fig.1 has been obtained by inserting the value of  $\mathcal{C}$  and  $\phi_{beg}$  at the onset of the  $R$ -boost.

Note that the scaling as  $1/a^2$  is sensibly different from a truly kinetic dominated phase in minimally coupled models, for which we should have had  $1/a^6$ , from the continuity equation (7) with  $p_\phi \simeq \rho_\phi$ . The reason why we have a different scaling of  $\rho_\phi$  is that the NMC terms in  $\tilde{\rho}_\phi$  are not negligible during all the RDE and the first part of the MDE, as we will show in a moment. Let us conclude the description of the  $R$ -boost by estimating the time of its end. The latter occurs at a redshift  $z_{pot}$  when the true potential energy becomes comparable with the kinetic energy (39):

$$\frac{1}{2}\phi_{beg}^2 \mathcal{C}^2 (1+z_{pot})^2 = V[\phi(z_{pot})] . \quad (40)$$

Since the  $R$ -boost is a very high redshift process, it covers a very tiny time interval, and in practice  $\phi$  does not move substantially from its initial condition  $\phi_{beg}$  during this phase. Therefore we can take  $V[\phi(z_{pot})] \simeq V(\phi_{beg})$  in Eq.(40). Moreover, for our inverse power-law potential we have  $V(\phi_{beg}) = V(\phi_0)(\phi_0/\phi_{beg})^2$ , and from the Friedmann equation today  $8\pi G V(\phi_0)/3 = \Omega_\phi H_0^2$ . Putting these ingredients together we can write an approximate formula for  $1+z_{pot}$  giving the end of the  $R$ -boost:

$$1+z_{pot} \simeq \sqrt{\frac{6\Omega_\phi H_0^2 \phi_0^2}{8\pi G \mathcal{C}^2 \phi_{beg}^4}} \simeq 3000 , \quad (41)$$

where the precise number has been obtained by making use of the actual value of the parameters in our case: it correctly corresponds to the  $R$ -boost end in Fig.1. Note that the end of the  $R$ -boost actually occurs when the Universe has already become matter dominated.

Before concluding this subsection, let us return to the importance of the NMC terms in  $\tilde{\rho}_\phi$  in equation (19); as we already anticipated, we show now that they are dominant with respect to kinetic and potential energy densities until the first part of the MDE. Indeed, the NMC term in  $\tilde{\rho}_\phi$  is  $-3\mathcal{H}F_\phi \dot{\phi}/a^2$  and scales roughly as  $1/a^3$ , since  $\mathcal{H}$  goes like  $1/a$ ; on the contrary, the true potential  $V$  is roughly constant and the  $R$ -boost kinetic energy scales like  $1/a^2$ ; as we explained. Because of these scalings, we expect that there exists a time  $\tau_{NMC}$  such that for  $\tau < \tau_{NMC}$  the NMC term is larger than both the kinetic and potential energy, while it becomes subdominant after this time. In fact, assuming that the time dependence of the field is as in the  $R$ -boost solution (38), a simple calculation shows that the NMC energy density term  $-3\mathcal{H}F_\phi \dot{\phi}/a^2$  dominates  $\rho_\phi$  up to

$$\tau_{NMC} \simeq \left[ \frac{3\xi \mathcal{C} \phi_{beg}^2}{\Omega_\phi \rho_{r0} H_0^3} \left( \frac{\phi_{beg}}{\phi} \right)^2 \right]^{1/3} \quad \text{or} \quad 1+z_{NMC} \simeq 850 , \quad (42)$$

that is long after matter radiation equivalence, as it is evident in Fig.1. Note however that this is only an approximation, since Eq.(41) tells us that the  $R$ -boost solution is no longer satisfied at these redshifts; anyway this clearly shows that the NMC terms become subdominant only after the onset of the matter domination, so that the distinction between  $\rho_\phi$  and  $\tilde{\rho}_\phi$  can be relaxed after  $\tau_{NMC}$ . Our analysis is therefore approaching the MDE behavior of  $\phi$ , subject of the next subsection.

### B. TEQ-trajectories in the Matter Dominated Era

Tracking solutions have been recently obtained in the context of Induced Gravity models [24], whose only difference compared with NMC is the absence of a constant term multiplying the Ricci scalar in the gravitational sector of the Lagrangian, i.e.  $F(\phi) = \xi\phi^2$ . We make two claims here. The first is that the same tracker solutions also exist in NMC models, provided in the MDE the scale factor can be expressed as a power of  $\tau$ . The second is that for  $F(\phi) \propto \phi^\beta$  the same solutions exist only if  $\beta = 2$ , as assumed so far.

In fact, by looking at Eqs.(4, 6), it is immediately realized that the difference between the IG and NMC models resides only in the  $1/3F$  term multiplying the RHS in (4), since all the other terms involving  $F$  are derivatives with respect to either time or  $\phi$ . Tracking solutions in [24] have been obtained by assuming that the scale factor in the MDE is the square of the conformal time  $\tau$ ,

$$a(\tau) = a_* \left( \frac{\tau}{\tau_*} \right)^2, \quad (43)$$

( $\tau_*$  is a generic time) so that Eq.(4) gets almost identically satisfied and disappears from the treatment. Indeed we show that in NMC models both Eq.(4) and Eq.(43) hold true, simply because matter is dominating and  $F(\phi)$ , playing the role of the gravitational constant in Eqs.(4, 5), is slowly moving. Since  $\phi_{beg} \ll \phi_0 \simeq 0.35M_P$ , it is easy to see that the variation of the value of  $F$  throughout the whole cosmological trajectory is <sup>1</sup>

$$\left| \frac{F_0 - F_{beg}}{F_0} \right| \simeq 4.6 \times 10^{-2}. \quad (44)$$

To see this in another way, Fig.3 shows the behavior of  $\mathcal{H}$ , indicated on the vertical axis as  $(1+z)H^{-1}$ , where  $H = a_t/a$ , in three important moments of the cosmological evolution, namely present (top), decoupling (middle), and equivalence (bottom); the heavy, solid line represents TEQ with positive  $\xi$ , the thin solid line is TEQ with negative  $\xi$ , the short dashed line, instead, is ordinary Q, and the long dashed one is the cosmological constant, which is sensibly different from Q and TEQ since it is not dynamical. As it is evident, opposite signs of  $\xi$  imply opposite behaviors for  $\mathcal{H}$ , especially at small redshifts, compared with ordinary Q. At a given redshift, the shift in  $\mathcal{H}$  is due to the behavior of  $F(\phi)$ , which is less or more than  $1/8\pi G$  for positive or negative  $\xi$ , respectively, by an amount given by (44).

Therefore, Eq.(43) holds with good accuracy, and all the solutions obtained in [24] for IG models, as well as their stability properties, hold true also in our NMC case.

Let us come now to our second claim. Let us assume for a while a form  $F(\phi) = \tilde{\xi}\phi^\beta$  and  $F(\phi) = 1/(8\pi G) + \tilde{\xi}(\phi^\beta - \phi_0^\beta)$ , respectively. We are searching for power law solutions for the Quintessence

$$\phi(\tau) = \phi_* \left( \frac{\tau}{\tau_*} \right)^\gamma; \quad (45)$$

from (43) and (45), it is matter of simple algebra to check that Eq.(6) takes the form

$$(\gamma^2 - \gamma) \frac{\phi}{\tau^2} = \frac{a^2 R}{2} \beta \tilde{\xi} \phi^{\beta-1} + a^2 \alpha \frac{M^{4+\alpha}}{\phi^{\alpha+1}}. \quad (46)$$

Also, from (9) the Ricci scalar in the MDE becomes  $R = 12/(a \cdot \tau)^2$ . It is easy to see that this is only satisfied if

---

<sup>1</sup>It is also useful to point out here that, because of the small change in the value of  $F(\phi)$  throughout the entire cosmological evolution, the well-known constraints on the variation of  $H$  at the epoch of nucleosynthesis are always satisfied in our models (see e.g. [13] and references therein).

$$\beta = 2 \text{ and } \alpha = \frac{6}{\gamma} - 2 . \quad (47)$$

This proves our second claim. If conditions (47) are satisfied, Eq.(46) gives  $\phi_*$  in terms of  $\gamma, n, \alpha$ ; since it must be positive, the following additional condition is derived:

$$\gamma^2 - \gamma - 12\tilde{\xi} > 0 . \quad (48)$$

In this regime, the Quintessence energy density scales as

$$\rho_\phi = \rho_{\phi*} \left( \frac{a}{a_*} \right)^{-\epsilon} , \quad \epsilon = \frac{3\alpha}{\alpha + 2} , \quad (49)$$

and its pressure is

$$p_\phi = -\rho_\phi \frac{2}{\alpha + 2} . \quad (50)$$

For what concerns the stability of these solutions, we report here only a remarkable result [24]; solutions satisfying (47) are stable under time dependent perturbations if and only if the following condition holds:

$$-1 - \frac{4}{\alpha + 2} < 0 , \quad (51)$$

holding for instance for any  $\alpha > 0$ . In summary, for the class of solutions we are interested in, namely those satisfying (43,46), the cases of interest here have been treated in [24]; we have shown here that such solutions apply both to NMC and IG cases.

Let us describe now in detail the solutions we see in Fig.1. Let us focus on the minimal coupling case first. The lowest, dashed line represents a minimally coupled case in which the behavior of the Q component during RDE is equivalent to a pure cosmological constant. The kinetic energy density is initially zero and remains largely subdominant with respect to the potential one. Thus  $\phi$  “freezes” for almost all the RDE, and leaves this condition only when its energy density reaches a fraction of about  $10^{-3}$  of the critical one. Thereafter, Q joins the tracker solution in the MDE regime corresponding to

$$\gamma = \epsilon = 1.5 , \quad (52)$$

that satisfies the constraint (48) with  $\tilde{\xi} = 0$ . The substantial motion of the field from the initial condition to its final value occurs in this last phase.

The thin long-dashed line represents a case in which the initial kinetic energy density is dominant with respect to the potential one, by 23 orders of magnitude. As it is evident, the field starts from an energy density comparable with the matter one. In this case the kinetic energy is redshifted away during the phase corresponding to the rapidly decreasing part of the trajectory in the figure; the scaling is easily found from the continuity equation, with  $\rho_\phi \simeq p_\phi$ . Then the field freezes again before joining the tracker solution at  $1 + z \simeq 100$ . Note that because of this early stage of kinetic energy dominance, the field freezes at a value slightly greater than the initial condition  $\phi_{beg} = 10^{-2}$ ; that is the reason why the flat part of the curve lies slightly below that corresponding to the previous case. Although not plotted in the figure, a roughly equivalent trajectory might have been obtained by requiring that the initial potential energy density was comparable to the matter one. Note the very large set of initial energy values from which the field reaches the present state.

Let us come now to the analysis of the tracker solutions in the NMC case. The heavy solid line has been obtained for  $\xi = 1.5 \times 10^{-2}$ . The RDE is dominated by the  $R$ -boost: the field accelerates until the gravitational effective potential is reached by the cosmological friction term in the Klein-Gordon equation. The slow rolling sets in, and holds until the true potential becomes important, when the field freezes. After this early phase,  $\tilde{\rho}_\phi$  and  $\rho_\phi$ , after having been much different in magnitude and sign, become indistinguishable, and join the tracker solution in the MDE reaching the required value today.

The heavy dashed line corresponds to a case in which the initial kinetic energy density is larger by 23 orders of magnitude with respect to the potential one, thus starting from an energy amount comparable with the matter one. As for the Q case, in this condition the field undergoes an era of kinetic energy dominance until the latter is redshifted below the effective NMC potential energy and the  $R$ -boost is set also in this case. The evolution of the field from this time on is the same as in the zero initial kinetic energy case.

The dot-dashed line is in fact the  $R$ -boost approximate solution (36). Note that it describes very well the  $R$ -boost, and shows as the terms of order higher than the first in Eq.(38) become important only now, when the  $R$ -boost is no longer active.

The last point we want to stress, is that the heavy solid line is actually superposed with a solid thin line, which describes a case identical, but for negative coupling constant,  $\xi = -1.5 \times 10^{-2}$ . The reason why these two trajectories agree so tightly is that during the  $R$ -boost the kinetic energy density, which dominates  $\rho_\phi$ , is the same regardless of the sign of  $\xi$ , see Eqs. (36- 39). The only slight difference between the two trajectories is when the  $R$ -boost ends and the true potential starts to drive the dynamics of  $\phi$ . For positive  $\xi$ ,  $\dot{\phi}$  is positive during the  $R$ -boost and later, while, for negative  $\xi$ ,  $\dot{\phi}$  is negative during the  $R$ -boost. Although the curves describing  $\rho_\phi$  for positive and negative values of  $\xi$  look very similar, this is not true for the perturbations they generate, as will be discussed in the next section.

#### IV. COSMIC MICROWAVE BACKGROUND SPECTRA

In this section we analyse the CMB temperature and polarization spectra of our TEQ model.

In Fig.4 we plot the CMB spectra for the models discussed in the previous section; the top panel describes temperature fluctuations; the bottom panel shows polarization spectra. The CMB spectrum coefficients are calculated from

$$C_\ell^T = 4\pi \int \frac{dk}{k} |\Delta_{T\ell}(k, \tau_0)|^2 , \quad C_\ell^P = 4\pi \int \frac{dk}{k} |\Delta_{P\ell}(k, \tau_0)|^2 , \quad (53)$$

where the quantities  $\Delta_{T\ell}(k, \tau_0)$  and  $\Delta_{P\ell}(k, \tau_0)$  are functions of the photon and baryon perturbed quantities, see e.g. ref. [10] for detailed definitions. The spectra have been normalized at the COBE measurements at  $\ell = 10$ .

The heavy, solid line in Fig.4 describes CMB spectra for the model corresponding to the same line in Fig.1. The thin, solid line describes the same model, but for  $\xi = -1.5 \times 10^{-2}$ , again as the same line in Fig.1. The short-dashed line, in the left panels, represents a case of ordinary Quintessence with the same potential and  $\Omega_\phi = 0.7$ . The long-dashed line, in the right panels, describes a cosmological constant,  $\Lambda$  model, with  $\Omega_\Lambda = 0.7$ . Before entering into the description of the various effects we find, let us stress that the effects of TEQ are quite large, with respect to both ordinary Q and  $\Lambda$  models. Also, the models plotted respect the experimental constraints discussed in Section II, having  $\omega_{JBD} \simeq 500$  and  $G_t/G \simeq 10^{-12} \text{ yr}^{-1}$ . We want to mention that the effects are here considerably larger than what we obtained in our previous paper [13]; the reason is twofold, in [13] we did not follow the tracker solution for the Q field, but for the shallower potential we considered there ( $\alpha = 1$ ) the size of the effects we find here would have been smaller anyway (see the discussion in Section VI).

First of all, let us consider the dynamics of Q at low redshifts. By looking at Eq.(6), it is easily seen that at present Q obeys a sort of effective potential, caused by the true potential and by the curvature-coupling term:

$$V_{eff}(\phi, R) = V(\phi) - \frac{F(\phi)R}{2} . \quad (54)$$

At low redshifts when Q starts to dominate, the dynamics of the Hubble length is suppressed since the universe is approaching a de Sitter phase. Therefore, by neglecting  $\dot{H}$  in Eq.(9), we have  $R \simeq 6H^2$ . Also, from the Friedmann equation we get  $(8\pi G/3)V \simeq \Omega_\phi H^2$ , and for inverse power-law potentials of the form (16) we have  $dV/d\phi = -\alpha V/\phi$ . Thus the derivative of the effective potential (54) takes the following approximate form:

$$\frac{dV_{eff}}{d\phi} \simeq - \left( \frac{3\alpha\Omega_\phi}{8\pi G\phi} + 6\xi\phi \right) H^2 ; \quad (55)$$

for positive  $\xi$ , both terms push toward increasing values of  $\phi$ , and we can immediately understand that the NMC term is comparable to the ordinary Quintessence one for

$$|\xi| = \frac{\alpha\Omega_\phi}{16\pi G\phi^2} . \quad (56)$$

Therefore, for  $\xi = 1.5 \times 10^{-2}$  and  $\alpha = 2$ , we expect to have a 10% extra force coming from the NMC terms in Eq.(4). Just the opposite happens if  $\xi$  is negative, since the terms in (55) have opposite sign. Indeed what we see in Fig.3 is that for opposite signs of  $\xi$ , the change in the low redshift dynamics of  $\mathcal{H}^{-1}$  is also opposite. Also, in Fig.2 it can be seen that at present roughly an order of magnitude separates the gravitational effective potential from the true one.

The Integrated Sachs Wolfe effect (ISW, see e.g. [31] for a review) makes the CMB coefficients on large scales, or small  $\ell$ 's, change with the variation of the gravitational potential along the CMB photon trajectories. Since the gravitational potential is affected by the low redshift dynamics, we expect an increase or a decrease of the ISW for positive and negative  $\xi$ , respectively. Indeed this is precisely what we see in Fig.4, looking at the curves for  $\ell \lesssim 10$ : positive or negative  $\xi$  TEQ make the  $C_\ell$  larger or smaller than ordinary Q, respectively.

The following simple calculation gives a good estimate of the amount of ISW in TEQ models. Take a cosmological scale comparable with the Hubble horizon today, so to be unaffected by acoustic oscillations. As it is known (see e.g. [31] and references therein), the ISW is simply given by the change, between decoupling and now, of the quantity  $\Psi - \Phi$ , where  $\Psi$  and  $\Phi$  are the gauge-invariant expressions of the gravitational potential and of the intrinsic spatial curvature, respectively; it can be seen [31] that this results in a fraction of  $\Psi - \Phi$  calculated at decoupling:

$$\left(\frac{\delta T}{T}\right)_{ISW} \propto (\Psi_{dec} - \Phi_{dec}) . \quad (57)$$

In NMC theories  $\Psi_{dec}$  and  $\Phi_{dec}$  are slightly different from those calculated in minimally coupled theories, because they receive a contribution from the time variation of the gravitational constant; since  $\Psi$  and  $\Phi$  are proportional to  $G \propto 1/F$ , in the limit  $|F_{dec} - F_0| \ll F_0$  they change by an amount  $(\Psi_{dec} - \Phi_{dec}) \cdot (1 - F_{dec}/F_0)$ . This induces an ISW effect which is

$$\left(\frac{\delta T}{T}\right)_{ISW,NMC} \propto (\Psi_{dec} - \Phi_{dec}) \cdot \left(1 + \frac{F_0 - F_{dec}}{F_0}\right) . \quad (58)$$

Therefore, on the CMB power spectrum, the NMC contribution to the ISW can be estimated as

$$\frac{\delta C_{\ell \lesssim 10}}{C_{\ell \lesssim 10}} = \frac{C_{\ell \lesssim 10}^{TEQ} - C_{\ell \lesssim 10}^Q}{C_{\ell \lesssim 10}^Q} = \frac{(\delta T/T)_{ISW,NMC}^2 - (\delta T/T)_{ISW}^2}{(\delta T/T)_{ISW}^2} \simeq 2 \cdot \frac{F_0 - F_{dec}}{F_0} \simeq 16\pi G \xi \phi_0^2 ; \quad (59)$$

the last equality has been obtained in our particular model, where at decoupling  $\phi \ll \phi_0$ , so that  $1 - F_{dec}/F_0 \simeq 8\pi G \xi \phi_0^2$ . Note again that, depending on the sign of  $\xi$ , the net effect can be an increase or a decrease of the CMB power. Indeed in Fig.3 we see that the above estimate is fairly well respected: since in the present case  $\phi_0 \simeq 0.35 M_P$  on large angular scales Eq.(59) predicts an effect of the order of 10%, as in the figure.

Let us come now to the evaluation of the effects on the acoustic peaks in the CMB spectrum. There are essentially two effects, peaks amplitude and position, that we describe now.

The amplitude changes in the opposite way for opposite sign of  $\xi$ . This feature can be understood as a normalization effect: we have seen that positive and negative  $\xi$  give rise to increased and decreased ISW in TEQ with respect to Q models; correspondingly, when the spectra are normalized at  $\ell = 10$ , a decrease and increase of the acoustic peak amplitude occurs. As a consequence, the magnitude of this effect is roughly at the level given by Eq.(59). For completeness, we report also another mechanism that changes the acoustic peaks amplitude, which occurs at decoupling, instead of at low redshifts. As is evident in Fig.3, the size of the Hubble horizon at a given redshift is different in TEQ with respect to Q models. As we noted in [13], this implies that the horizon reentry for a given comoving scale is delayed for positive  $\xi$  and anticipated for negative  $\xi$ ; therefore, with respect to the ordinary tracking Quintessence, this implies a slight excess or deficit in CDM density when such scale is in horizon crossing, corresponding to a deficit and an excess in the radiation energy density. This slightly suppresses the acoustic oscillations in the first case, and enhances them in the second.

Let us come now to the explanation of the acoustic peaks shift. The angular scales at which acoustic oscillations occur are directly proportional to the size of the CMB sound horizon at decoupling, that in comoving coordinates is roughly  $\tau_{dec}/\sqrt{3}$ , and inversely proportional to the comoving distance covered by CMB photons from last scattering until observation, that is  $\tau_0 - \tau_{dec}$  [31]. Therefore, since the spectrum multipoles scale as the inverse of the corresponding angular scale, we have

$$\ell_{peaks} \propto \frac{\tau_0 - \tau_{dec}}{\tau_{dec}} . \quad (60)$$

In our models,  $\tau_0$  and  $\tau_{dec}$  shift essentially because of two reasons, namely the change in  $\tau_0$  due to the domination of the Q component today, and the behavior the Hubble length  $H^{-1}$  in the past. The first feature mainly makes the Q and TEQ models different from a cosmological constant, since the latter does not have the kinetic degree of freedom. The second feature is simply related to the fact that, for a fixed value of the Hubble length today, in the past it possesses a behavior which is characteristic of the particular model at hand, because of the time evolution of the effective gravitational constant  $1/F(\phi)$  (see Fig.3). Let us give a simple analytical formula for the acoustic peaks shift in TEQ models with respect to ordinary tracking Q. First, it can easily be seen that the conformal time  $\tau$  can be conveniently written as a function of the scale factor as follows:

$$\tau = \int_0^a \frac{da}{a\dot{a}} . \quad (61)$$

However, from the Friedmann equation (4),  $\dot{a}$  scales as the inverse of  $\sqrt{F}$ ; therefore, small changes  $\delta F \ll F$  induce a change  $\delta \dot{a}/\dot{a} \simeq -(1/2)\delta F/F$ , and consequently in the conformal time, which shifts by an amount

$$\delta\tau = \int_0^a \frac{da}{a\dot{a}[1 - (1/2)\delta F/F]} - \tau \simeq \frac{1}{2} \int_0^a \frac{da}{a\dot{a}} \frac{\delta F}{F} , \quad (62)$$

where we have defined the time change of  $F$  as follows:

$$\frac{\delta F}{F} = \frac{F(\phi) - F_0}{F_0} . \quad (63)$$

Of course  $\delta F/F$  at any given time depends on various details, but let us make the simplifying assumption that it is constant from the beginning until  $z = 2$  and zero afterwards, empirically following what we see in Fig.3. It is then immediate to deduce that  $\tau_{dec}$  changes as

$$\delta\tau_{dec} \simeq \tau_{dec} \cdot \frac{1}{2} \frac{\delta F}{F} . \quad (64)$$

Instead, for what concerns  $\tau_0$  we have

$$\delta\tau_0 \simeq \tau_{z=2} \cdot \frac{1}{2} \frac{\delta F}{F} , \quad (65)$$

because, according to our simplifying assumption,  $\delta F/Fa \approx 0$  for  $z \lesssim 2$ . In conclusion, minding Eq.(60), and after some algebra, we get the shift in the acoustic peaks as a result of the time variation of the effective gravitational constant:

$$\frac{\delta l_{peaks}}{l_{peaks}} = \frac{l_{peaks}^{TEQ} - l_{peaks}^Q}{l_{peaks}^Q} \simeq \frac{1}{2} \frac{\delta F}{F} \left( \frac{\tau_{z=2}}{\tau_0} - 1 \right) . \quad (66)$$

Numerically we find  $\tau_{z=2}/\tau_0 \simeq 75\%$ ; also, we already mentioned that the change of the value of  $F$  during all the cosmological evolution can be written as  $\delta F/F \simeq -8\pi\xi G\phi_0^2$ . Therefore, for our specific model Eq.(66) becomes

$$\frac{\delta l_{peaks}}{l_{peaks}} \simeq \pi\xi G\phi_0^2 . \quad (67)$$

Note that, for our values of  $\xi = \pm 1.5 \times 10^{-2}$ , the above shift is at the level of  $\pm 6 \times 10^{-3}$ , which is in quite good agreement with the results plotted in the left panels of Fig.4, that is  $\pm 5 \times 10^{-3}$ .

This completes our description of the TEQ features on the CMB angular power spectrum. We turn now to the analysis of what happens in the matter power spectrum today.

## V. MATTER POWER-SPECTRUM

In Fig.5 we plot the matter power spectrum for the same cases shown in Fig.4. We can note immediately differences regarding both amplitude and turnover position.

The  $\Lambda$  model has the highest spectrum. The main reason is the different growth of density perturbations [6]. In both  $Q$  and  $\Lambda$  models the perturbation growth is suppressed at low redshifts due to the domination of the vacuum energy, that tends to keep  $\dot{H}$  constant therefore enhancing the cosmological friction in the perturbation equations, where almost everywhere the terms involving the first time derivatives of the perturbations appear multiplied by the Hubble parameter. In  $Q$  and TEQ models this effect is considerably enhanced due to the magnitude of  $\dot{H}$  which is greater than in  $\Lambda$  models at all redshifts, and in particular at the lowest ones, as it is evident from Fig.3. Another independent cause that contributes to push the  $Q$  spectrum down with respect to the  $\Lambda$  model is the COBE normalization. In fact, we have seen that the ISW effect is enhanced in  $Q$  models with respect to  $\Lambda$  ones, and the normalization to COBE implies subtraction of power to the true amplitude of the primordial cosmological perturbations.

Let us come now to the difference between  $Q$  and TEQ models. The dynamics of the field at low redshifts is almost the same as in  $Q$  models, as it is evident again by looking at Fig.1. Thus, the reason of the difference is to be searched for in the COBE normalization. Indeed, by looking at the low wavenumber region, which is the zone of non-processed scales, we see that the amplitude shift is roughly at 10% and  $-18\%$  level for TEQ with respect to  $Q$  for negative and

positive  $\xi$ , respectively; these numbers roughly agree with the ISW corrections that we estimated to come from the NMC terms in the previous section.

Let us come now to the evaluation of the peaks shifts. As it is known (see for example [6]), the scale of the matter power spectrum turnover is essentially given by the scale entering the Hubble horizon at the matter-radiation equivalence. The latter age is the same for all our models:

$$1 + z_{eq} = \frac{\rho_{m0}}{\rho_{r0}} \approx 5500 . \quad (68)$$

However, we must take care of what was the Hubble horizon at the equivalence, since the Hubble radius follows different dynamics in the three cases that we are treating. In other words, the shift in the power spectrum turnover is given by

$$\frac{\delta k_{turn}}{k_{turn}} = - \left( \frac{\delta H^{-1}}{H^{-1}} \right)_{eq} . \quad (69)$$

In Fig.3 the different values of the Hubble horizon are displayed at the equivalence (bottom). The Hubble horizon shift in Eq.(69) between the Q and  $\Lambda$  model is at the 18% level, which corresponds well to the power spectrum shift that we see in Fig.5, where  $\delta k_{turn}/k_{turn} \simeq -20\%$ . The same reasoning applies to explain the slight shift of the TEQ spectra turnover with respect to the Q one. The Hubble horizon shift in Fig.3 for positive  $\xi$  is 2.6%, in good agreement with what we get in Fig.5, 2.3%; for negative  $\xi$  we get 1.7% from both figures.

We can give a rough analytical estimate of this effect by reasoning as follows. At the equivalence the Q energy density, both in Q and TEQ models, is negligible with respect to matter and radiation as it is evident in Fig.1. Eq.(4) takes the form

$$\mathcal{H}^2 \simeq \frac{\rho_{fluid}}{3F(\phi)} . \quad (70)$$

Since in our model  $F(\phi)$  is smaller or larger than  $F(\phi_0)$  if  $\xi$  is positive or negative, respectively, this implies that the Hubble length  $H^{-1}$  at the equivalence was different in TEQ models with respect to ordinary Q; the amount and the sign of the difference can be estimated roughly as follows: from Eq.(70) we have

$$\left( \frac{\delta H^2}{H^2} \right)_{eq} \simeq \left( \frac{2\delta H}{H} \right)_{eq} = 1 - 8\pi G \cdot F_{eq}(\phi_{eq}) . \quad (71)$$

Therefore, the matter power spectrum turnover shifts due to the NMC terms by the following amount:

$$\left( \frac{\delta k_{turn}}{k_{turn}} \right)_{NMC} = - \left( \frac{\delta H^{-1}}{H^{-1}} \right)_{eq} = \frac{1 - 8\pi G F_{eq}(\phi)}{2} \simeq 4\pi G \xi \phi_0^2 , \quad (72)$$

simply by taking  $\phi_{eq} \ll \phi_0$  as it is today. In our models, the quantity in Eq.(72) is roughly 2%, that agrees quite well with the numbers we obtain.

For what concerns the shape of the power spectrum, there is no significant differences between Q and TEQ models, since this could arise only when the scalar field becomes important at low redshifts, where however the dynamics in the two scenarios is very similar.

## VI. VARIATIONS IN THE POTENTIAL SLOPE

Varying the power  $\alpha$  in the potential (16) implies varying the dynamics of  $\rho_\phi$  according to Eq.(49). For increasing slopes of the potential, we expect that the low redshift effects are enhanced correspondingly.

In Fig.6 we show tracking solutions for different exponents: dot-dashed line for  $\alpha = 1$ , solid for  $\alpha = 2$ , long-dashed for  $\alpha = 3$ . It can be immediately seen how the low redshift tracker branch possesses different slopes, according to Eq.(49). Moreover, the  $R$ -boost is the same for all the slopes, again according to the arguments made in Section II. But, for increasing  $\alpha$ , the  $R$ -boost is abandoned earlier. The reason is the mechanism that stops the  $R$ -boost itself, i.e. the fact that the Q potential energy starts to dominate. But, this happens earlier for larger exponents in Eq.(16), since the potential is steeper for  $\phi < \phi_0$ .

Another important aspect that we must address is the Q equation of state,  $w_\phi = p_\phi/\rho_\phi$ , since this is a parameter that is quite well constrained by the observations to be less than  $-0.6$  today [1–3,8]. In fact, from Eq.(50) we see that small  $\alpha$  make the equation of state similar to the pure cosmological constant case. The actual value that we find numerically is slightly different from what Eq.(50) would predict, because today the tracker regime has been

abandoned, since  $Q$  has started to dominate the cosmic evolution. For  $\alpha = 1, 2, 3$ , we find  $w_\phi = -0.75, -0.60$  and  $-0.49$ , respectively, for positive  $\xi$ , and  $w_\phi = -0.78, -0.66, -0.59$ , respectively, for negative  $\xi$ .

Next, let us see what happens in the CMB. Fig.7 shows the behavior of the CMB temperature (top) and polarization (bottom) spectra for the same values of  $\alpha$  as in Fig.6; the left and right panels are for positive and negative  $\xi$ , respectively. Solid lines, both heavy and thin, refer to the same cases as in Fig.4; the dotted and dot-dashed lines describe models with  $\alpha = 3$  and 1, respectively. As we mentioned above, the low redshift ISW effect is enhanced by increasing  $\alpha$ , merely because the low redshift dynamics is enhanced, as it is evident from Eq.(55). This is a known effect since it does not involve directly NMC terms, but instead is a characteristic feature of dynamical vacuum energy models [4,5]. The acoustic peaks region is suppressed correspondingly, by an amount that is roughly increasing linearly with  $\alpha$ , due to the COBE normalization at low  $\ell$ 's. However, as it can be easily noted in Fig.7, the strength of this effect is larger for positive  $\xi$  compared with negative values. The reason is that negative  $\xi$  values tend to decrease the ISW effect, as it is evident both in the effective potential (55) and in our estimate of Eq.(59). For what concerns the shift in the position of the acoustic peaks, the different potential mainly influences the low redshift tracking behavior, thus affecting mostly  $\tau_0$  in (60); since large  $\alpha$  enhance the low redshift dynamics, the peaks shift increases correspondingly, again as it is evident in Fig.7.

In conclusion, the increased dynamics obtained by increasing  $\alpha$  has the indirect effect of enhancing all the NMC effects. To see this, let us stress the part of the effects that come from genuine NMC terms. To this aim we build tracking solutions corresponding to those that we show in Fig.6, but for the ordinary  $Q$  case, and calculate the CMB spectra for them. We take the ratios Eq.(59), now valid for all the  $\ell$ 's,

$$\frac{\delta C_\ell}{C_\ell} = \frac{C_\ell^{TEQ} - C_\ell^Q}{C_\ell^Q}, \quad (73)$$

to quantify in detail the pure NMC effects in the spectra. These quantities, for the different values of  $\alpha$  treated in this Section, are displayed as a function of the multipole  $\ell$  in Fig.8, temperature (top) and polarization (bottom). The meaning of the curves is the same as in Fig.7. The effects are larger for increasing values of  $\alpha$ . In the upper box we can note the large ISW effect due to the NMC component only: it reaches roughly 30% by itself. Correspondingly, due to the normalization at small  $\ell$ 's, the acoustic peaks region is suppressed or enhanced for positive or negative  $\xi$ , respectively, even up to the 50% level. The enhancement of these effects, in particular the ISW one, for increasing  $\alpha$  is in agreement with our formula (59), since for increasing  $\alpha$  the field reaches larger values today: namely, for  $\alpha = 1, 2, 3$ , we have  $\phi_0 = 0.2, 0.35$  and  $0.5$  Planck masses for positive  $\xi$ , and similar values for negative  $\xi$ .

The same phenomenology obtained for the temperature anisotropies is found for the polarization (bottom panels); we will not plot the low  $\ell$ 's region, since even if the NMC effect is large, the absolute value of the polarization multipole moments is significantly high only around degree angular scales.

## VII. CONCLUSIONS

In this section we will make a self consistent summary of the results obtained in this paper, focusing on the observable features of the cosmological models here investigated.

The present paper is devoted to the study of theoretical aspects and observational imprints of cosmological scenarios in which a dynamical vacuum energy component dominates the cosmic evolution today, as suggested by high-redshift type Ia Supernovae data [1].

Extended Quintessence means the class of models for which the vacuum energy today is given by a scalar field which has an explicit coupling with the Ricci scalar  $R$ ; we proposed this scenario in [13] and performed a preliminary study of its cosmological properties. In the present work we assume a Non-Minimal Coupling (NMC) term of the form

$$\frac{R}{16\pi G} + \xi (\phi^2 - \phi_0^2), \quad (74)$$

where  $\xi$  is a dimensionless coupling constant,  $\phi$  is the Quintessence field, also indicated by  $Q$ , and  $\phi_0$  is its value today.

As a first step, we investigated the cosmological trajectories in this scenario, focusing on the redshift evolution of the  $Q$  energy density. The  $Q$  potential is modeled as an inverse power law, namely  $V(\phi) = M^{4+\alpha}/\phi^\alpha$ , where  $\alpha > 0$  and  $M$  is the energy scale chosen to have the amount of  $Q$  energy today.

In the radiation dominated era we find that the divergence of  $R$  at early times generates an effective gravitational potential in the Klein Gordon equation, which drives the  $Q$  evolution in a sort of gravitational slow rolling. We named this era  $R$ -boost. The dominant component in  $\rho_\phi$  during this epoch is the kinetic component. The  $R$ -boost ends when this kinetic energy becomes comparable with the true potential energy: we have estimated that this time corresponds to a redshift  $1 + z_{pot} \simeq 3000$ , i.e. the  $R$ -boost lasts also for the earliest part of the matter dominated era.

In the matter dominated era we obtained scaling solutions in NMC theories, which extend the validity of those studied in [24], for which  $\rho_\phi$  and the Q pressure  $p_\phi$  scale as follows:

$$\rho_\phi = \rho_{Q0} \left( \frac{a_0}{a} \right)^\epsilon, \quad \epsilon = \frac{3\alpha}{\alpha+2}, \quad p_\phi = -\rho_\phi \frac{2}{\alpha+2}. \quad (75)$$

This regime holds for almost all low redshifts,  $1+z \lesssim 100$ . At recent times, however,  $1+z \lesssim 3$ , the Quintessence component starts to dominate and the expansion accelerates.

These results show that the Extended Quintessence is a tracker field, in the sense of the original works on Quintessence tracker solutions [7,9]. While the Quintessence potential energy density has to be chosen to produce the observed  $\Omega_\phi$  today, just as if Q was ordinary cosmological constant, the initial amount of  $\rho_\phi$  can vary over a very wide range, covering more than 20 orders of magnitude.

We also investigate perturbation spectra in TEQ. The tracker dynamics imprints considerably larger effects compared with ordinary Tracking Quintessence and the cosmological constant, both on CMB and LSS. We gave quite accurate analytical formulas to describe these effects, that we summarize here.

We have shown that in TEQ models the low redshift dynamics of the field is either increased or decreased depending on whether  $\xi$  is positive or negative, respectively. This leaves its imprints on the large scale CMB angular power spectrum, where the signal is unprocessed by acoustic oscillations, and is affected by the dynamics of the gravitational potential (Integrated Sachs Wolfe effect, ISW). We derived the following simple formula describing this effect. If  $C_\ell$  is the coefficient describing the power of CMB anisotropies on large angular scales,  $\ell \lesssim 10$ , the shift in TEQ models compared with ordinary Q is given by

$$\frac{\delta C_{\ell \lesssim 10}}{C_{\ell \lesssim 10}} \simeq 2(1 - 8\pi GF_{dec}), \quad (76)$$

where  $F$  is the NMC function in Eq.(74). because of the tracking regime we generally have  $\phi_{beg} \ll \phi_0$ , so that the above equation assumes the simple form

$$\frac{\delta C_{\ell \lesssim 10}}{C_{\ell \lesssim 10}} \simeq 16\pi G\xi\phi_0^2, \quad (77)$$

which means an effect going from 10 to 50% for the potential slope  $\alpha$  increasing from 1 to 3. Note that for negative  $\xi$  the ISW is inverted, a feature that is quite unusual in Quintessence models.

The amplitude of the acoustic peaks varies because of the same ISW effect, if the overall power is normalized to COBE at  $\ell = 10$ . There exists also another mechanism that changes the acoustic peaks amplitude, which occurs at decoupling rather than at low redshifts. The Hubble horizon value at a given redshift is different in Extended vs. ordinary Quintessence models, as already noticed in [13]. This is because in order to reach the same value today the Hubble parameter followed a different dynamics in the past; we have shown here that the horizon reentry for a given comoving scale is delayed for positive  $\xi$  and anticipated for negative  $\xi$ . This implies a slight suppression of the acoustic oscillations in the first case, and an enhancement in the second, as a consequence of the different amounts of CDM when the baryon and photon densities are oscillating.

TEQ imprints also affect the position of the acoustic peaks. The angular multipoles at which CMB acoustic oscillations are occurring are inversely proportional to the comoving size of the CMB sound horizon at decoupling, proportional to  $\tau_{dec}$ , and directly proportional to the comoving distance between last scattering and us,  $\tau_0 - \tau_{dec}$ . Both these quantities are affected by the TEQ dynamics. The CMB sound horizon is proportional to the Hubble horizon at decoupling, which, as we just mentioned is different in the various models. The comoving distance between last scattering and us is also affected by the TEQ low-redshift dynamics. We derived the following simple analytical formula giving the shift in the positions of the acoustic peaks, which accurately describes our numerical results:

$$\frac{\delta\ell}{\ell} \simeq \frac{8\pi GF(\phi_{dec}) - 1}{8} = \pi G\xi\phi_0^2. \quad (78)$$

Note that again, depending on the sign of  $\xi$ , Eq.(78) may imply a peak shift towards smaller or larger angular scales.

For what concerns the LSS effects today, the first point to make is that since at the COBE scales, where we normalize our models, the CMB spectrum is affected by the ISW, the amplitude of perturbations on LSS scales is suppressed if  $\xi > 0$  and increased if  $\xi < 0$ , by an amount that is approximately the opposite of the quantity in Eq.(77). Second, the turnover scale position  $k_{turn}$  is shifted, being inversely proportional to the Hubble horizon at the equivalence. The size of this effect can be simply estimated by the Friedmann equation:

$$\left( \frac{\delta k_{turn}}{k_{turn}} \right)_{NMC} = \frac{1 - 8\pi GF_{eq}}{2}. \quad (79)$$

Again, this is roughly  $4\pi G \xi \phi_0^2$  because, thanks to the tracking behavior,  $\phi_{eq} \ll \phi_0$ .

This completes the list of our main results. A very final comment we want to make is that CMB anisotropies have been shown here to be considerably affected by the dynamical properties of the vacuum energy and by the Non-Minimal Coupling terms present in the Lagrangian. This is an important novelty in the literature on Quintessence models, which deserves as much attention as the dependence of the CMB spectra on the kind of dark matter, value of the primordial perturbation spectral index, etc.. This is made possible by the fact that the CMB itself is more than a snapshot of the early universe; its properties in fact are also determined by a sort of line-of-sight integration over a very long part of the cosmic evolution, which is then able to tell us about the time variation of the gravitational constant and the dynamics of the vacuum energy.

With higher and higher accuracy achieved in CMB data, going from the encouraging, present-day ones [17,18] to the formidable performance of the Microwave Anisotropy Probe and Planck mission [16], we will be able to get exciting new insights into the structure of gravity as well as the nature of the vacuum energy.

#### ACKNOWLEDGMENTS

Matthias Bartelmann is warmly acknowledged for useful comments.

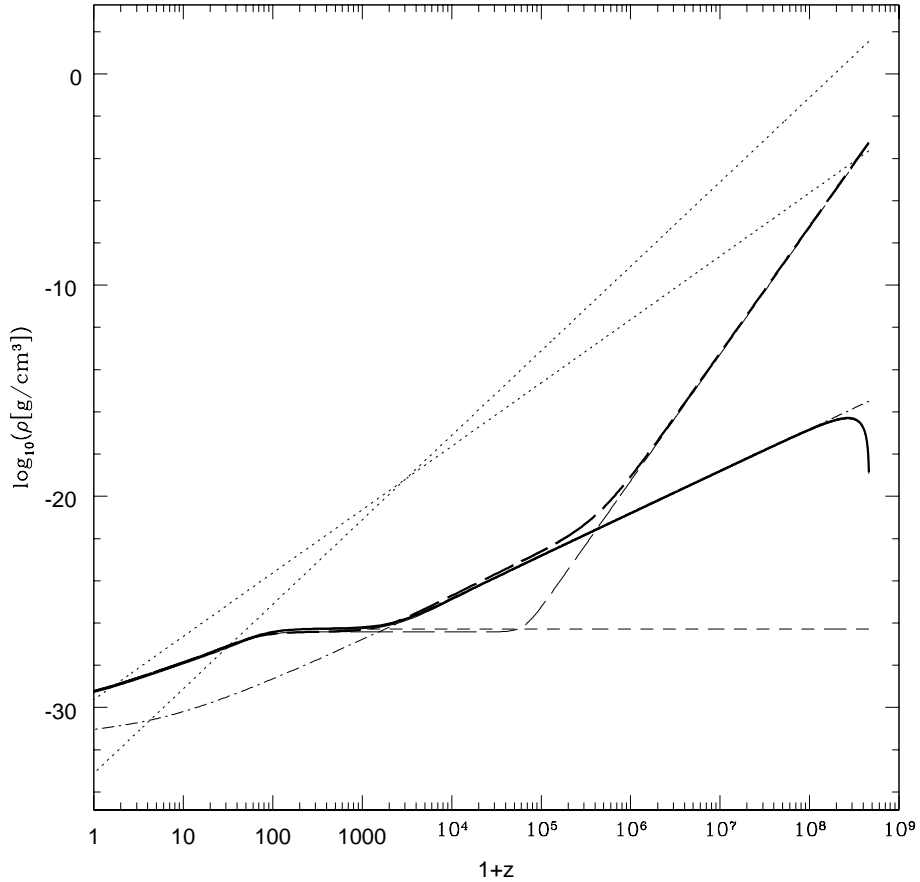


FIG. 1. Matter, radiation, Quintessence energy densities as functions of redshift. Dotted lines: matter and radiation; heavy solid: Tracking Extended Quintessence; thin dashed: tracking minimally coupled Quintessence; heavy dashed: initially highly energetic Tracking Extended Quintessence; thin long-dashed initially highly energetic tracking Quintessence; dot-dashed:  $R$ -boost analytic.

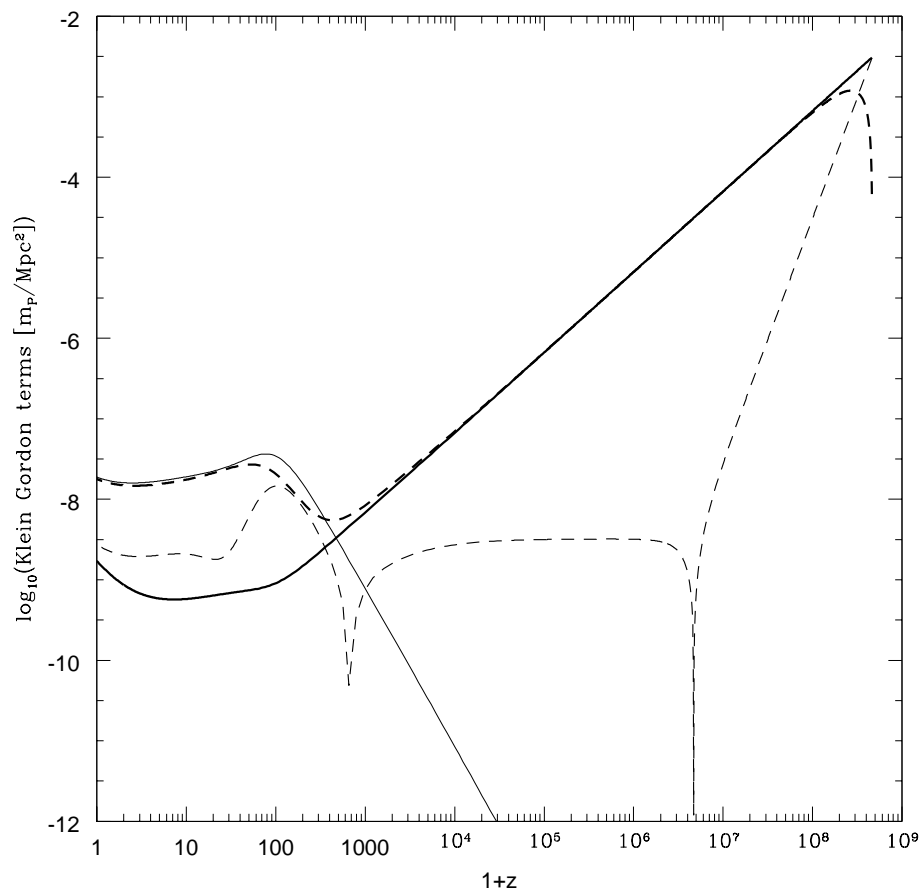


FIG. 2. Absolute value of the Klein Gordon equation terms: heavy solid: gravitational effective potential; heavy dashed: friction; solid: potential; dashed: acceleration.

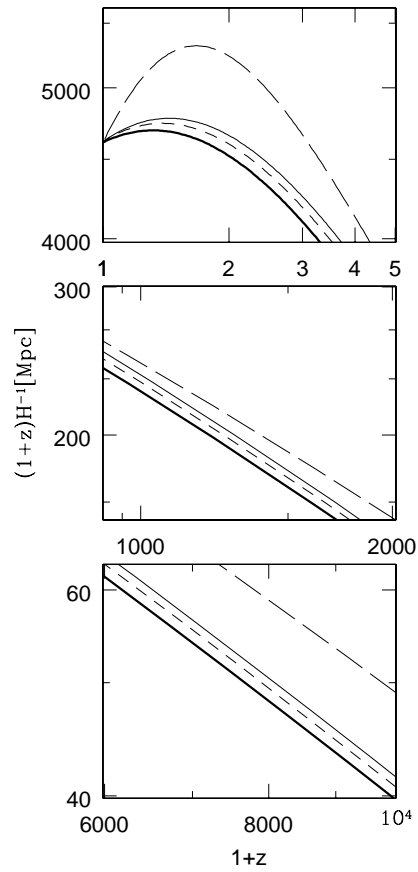


FIG. 3. Snapshots of conformal Hubble horizon evolution. heavy solid: Tracking Extended Quintessence with positive  $\xi$ ; short dashed: tracking minimally coupled Quintessence; thin solid: Tracking Extended Quintessence with negative  $\xi$ ; long dashed: cosmological constant. Top: present; middle: decoupling; bottom: equivalence.

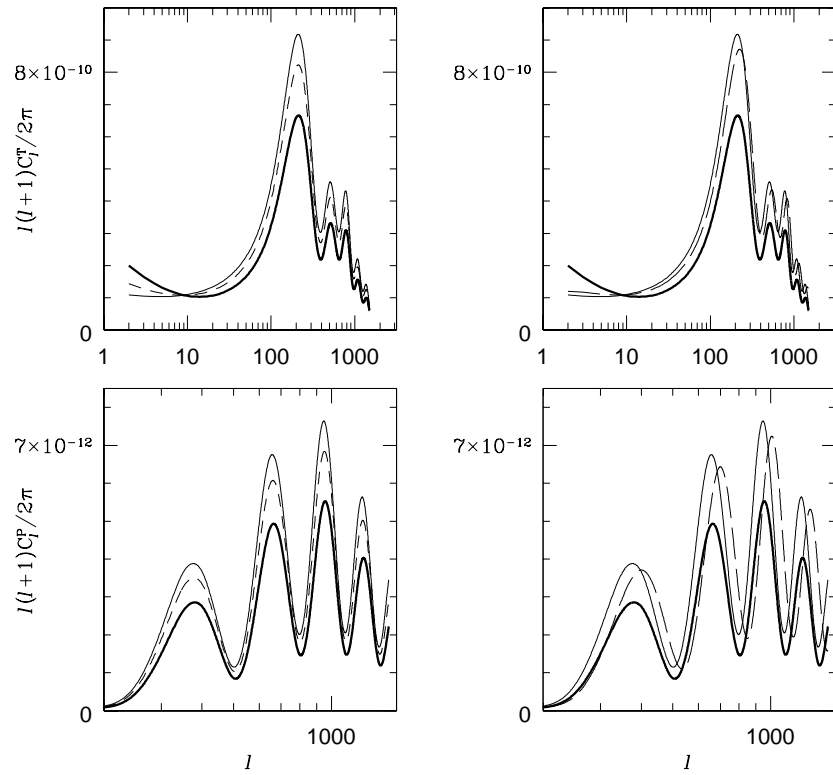


FIG. 4. CMB angular power spectra. Top: temperature; bottom polarization. Heavy solid: Tracking Extended Quintessence, positive  $\xi$ ; thin solid: Tracking Extended Quintessence, negative  $\xi$ ; short dashed: minimally coupled tracking Quintessence; long dashed: cosmological constant.

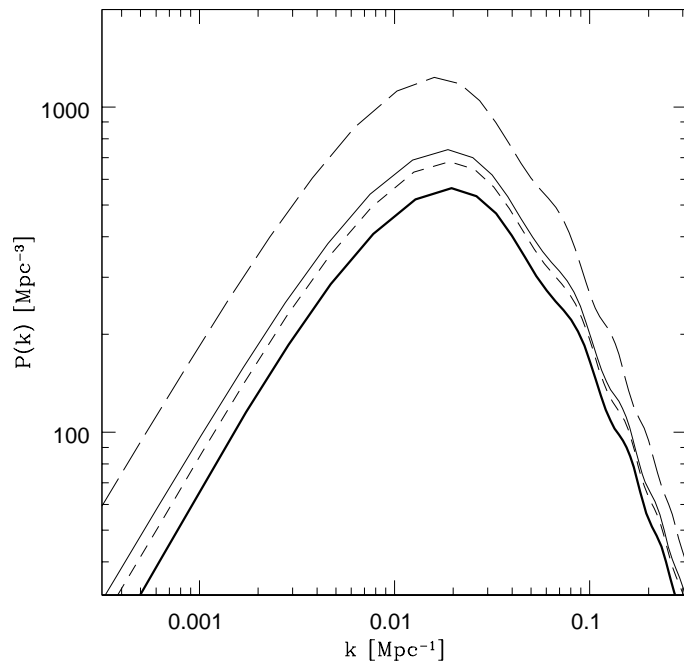


FIG. 5. Present matter power spectra. Heavy solid: Tracking Extended Quintessence, positive  $\xi$ ; thin solid: Tracking Extended Quintessence, negative  $\xi$ ; short dashed: minimally coupled tracking Quintessence; long dashed: cosmological constant.

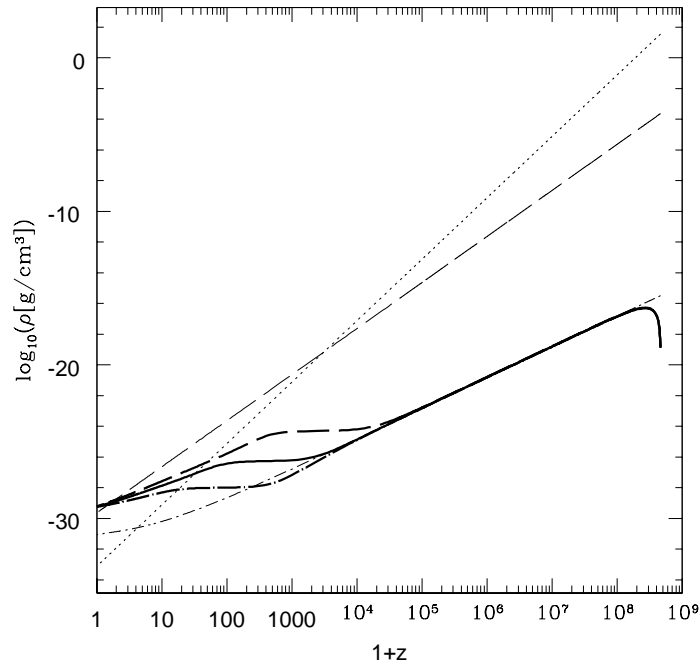


FIG. 6. Matter, radiation and Quintessence energy densities for different potential slopes. Long dashed: matter; short dashed: radiation; heavy solid: Tracking Extended Quintessence,  $\alpha = 2$ ; heavy dotted dashed: Tracking Extended Quintessence,  $\alpha = 1$ ; heavy long dashed: Tracking Extended Quintessence,  $\alpha = 3$ .

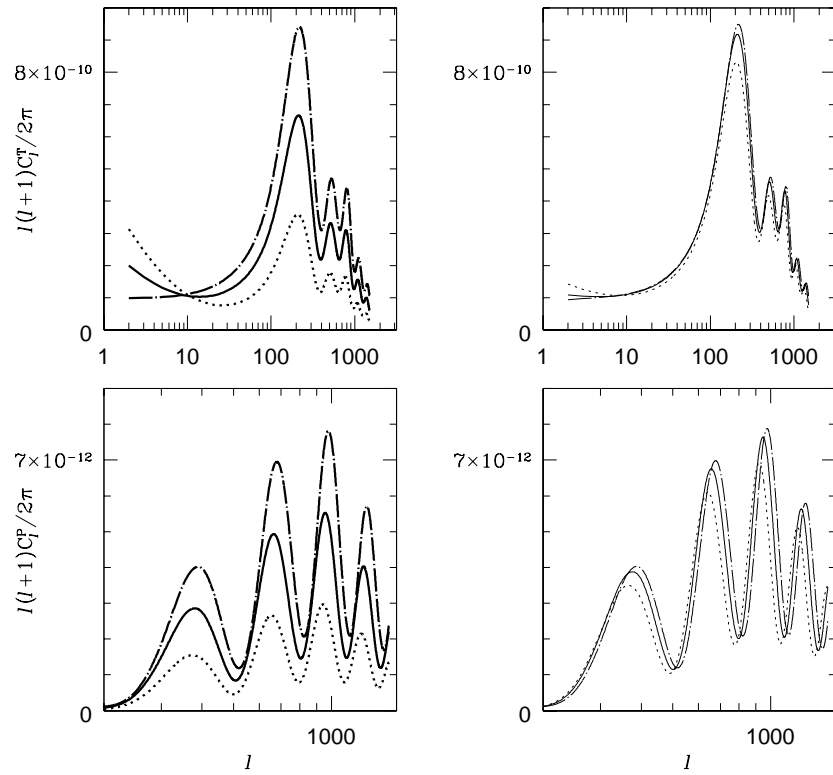


FIG. 7. CMB angular power spectra for different potential slopes. Left (right): positive (negative)  $\xi$ . Solid: Tracking Extended Quintessence,  $\alpha = 2$ ; dotted dashed: Tracking Extended Quintessence,  $\alpha = 1$ ; short dashed: Tracking Extended Quintessence,  $\alpha = 3$ .

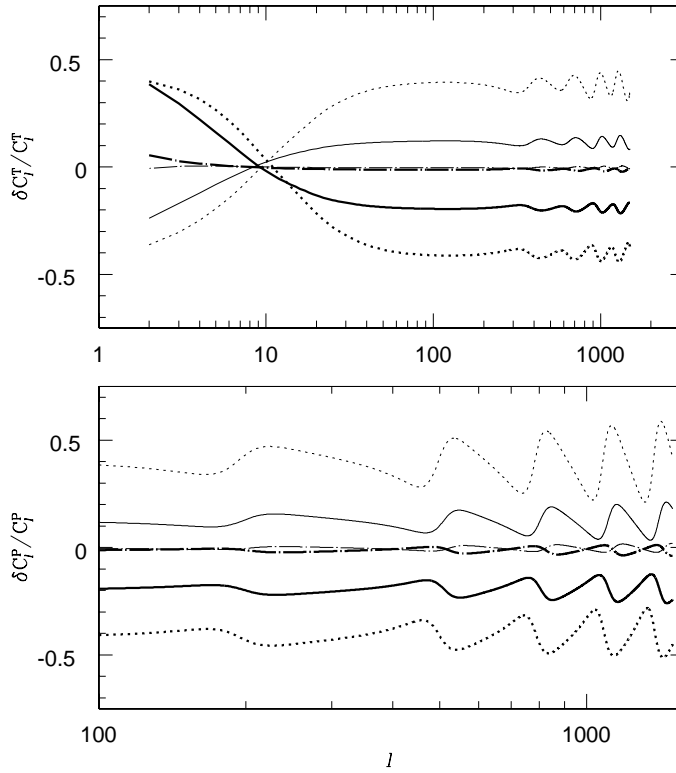


FIG. 8. CMB angular power spectra: relative difference between Tracking Extended Quintessence and ordinary tracking Quintessence spectra ( $\delta C_\ell = C_\ell^{TEQ}/C_\ell^Q - 1$ ) as a function of the inverse power of  $\phi$  in the potential. Top (bottom): temperature (polarization); thick (thin) lines for positive (negative)  $\xi$ . Solid: extended vs. ordinary tracking Quintessence,  $\alpha = 2$ ; dotted dashed for  $\alpha = 1$ , short dashed for  $\alpha = 3$ .

---

[1] S. Perlmutter, M.S. Turner & M. White, Phys.Rev.Lett. 83, 670 (1999)  
[2] A.G. Riess *et al.*, ApJ in press, preprint astro-ph/0001384  
[3] P. M. Garnavich *et al.*, Astrophys.J. 509, 74 (1998)  
[4] P.J. Peebles, B. Ratra, Astrophys. J. 352, L17 (1988); R.R. Caldwell, R. Dave, P.J. Steinhardt, Phys. Rev. Lett. 80, 1582 (1998).  
[5] P.G. Ferreira, M. Joyce, Phys. Rev. D 58 023503 (1998); P.T.P. Viana, A.R. Liddle, Phys. Rev. D 57, 674 (1998).  
[6] K. Coble, S. Dodelson, J. Friemann, Phys. Rev. D 55, 1851 (1997).  
[7] B. Ratra, P.J. Peebles, Phys. Rev. D 37, 3406 (1988).  
[8] G. Efstathiou, MNRAS 310, 842 (1999).  
[9] L. Wang, R. R. Caldwell, J. P. Ostriker, P. J. Steinhardt, Ap.J. 530 17-35 (2000), astro-ph/9901388. P.J. Steinhardt, L. Wang, I. Zlatev, Phys. Rev. D 59, 123504 (1999); I. Zlatev, L. Wang, P.J. Steinhardt, Phys. Rev. Lett. 82, 896 (1999); A.R. Liddle, R.J. Scherrer, Phys. Rev. D 59, 023509 (1999).  
[10] F. Perrotta, C. Baccigalupi, Phys. Rev. D 59, 123508 (1999).  
[11] S.M. Carroll, Phys. Rev. Lett. 81, 15, 3097 (1998).

- [12] L. Amendola, preprint astro-ph/9908023 (1999).
- [13] F. Perrotta, C. Baccigalupi, S. Matarrese Phys. Rev. D 61 023507 (2000), astro-ph/9906066
- [14] F. Zee, Phys. Rev. Lett. 42, 417 (1979).
- [15] N.D. Birrel, P.C. Davies, Quantum Fields in Curved Spaces, Cambridge Univ. Press, Cambridge (1982).
- [16] MAP home page: <http://map.gsfc.nasa.gov/> ;  
Planck Surveyor home page: <http://astro.estec.esa.nl/SA-general/Projects/Planck/>
- [17] P. de Bernardis *et al.* Nature 404, 955 (2000).
- [18] S. Hanany *et al.*, submitted to Ap.J.Lett., astro-ph/0005123 (2000).
- [19] D. La, P.J. Steinhardt, Phys. Rev. Lett. 62, 376 (1989); F.S. Accetta, J.J. Trester, Phys. Rev. D 39, 2854 (1989); E.J. Weinberg, Phys. Rev. D 40, 3950 (1989).
- [20] P. Jordan, Z. Phys. 157, 112 (1959); C. Brans, R.H. Dicke, Phys. Rev. 124, 925 (1959).
- [21] A.D. Dolgov, In *The Very Early Universe*, eds. G.W. Gibbons, S.W. Hawking, S.T.C. Siklos, Cambridge University Press, Cambridge, p. 449 (1983).
- [22] T. Chiba, Phys.Rev. D60 083508 (1999), gr-qc/9903094.
- [23] L. Amendola, Phys.Rev. D60 043501 (1999), astro-ph/9904120.
- [24] J.P. Uzan, Phys. Rev. D 59, 123510 (1999).
- [25] R. de Ritis, A. A. Marino, C. Rubano, P. Scudellaro, submitted to Physical Review D, hep-th/9907198 (1999).
- [26] N. Bartolo & M. Pietroni, Phys.Rev. D61 023518 (2000).
- [27] J.C. Hwang, ApJ 375, 443 (1991); J.C. Hwang, Phys. Rev. D 53, 762 (1996); J.C. Hwang, Class. Quantum Grav. 7, 1613 (1990).
- [28] G.T. Gillies, Rep. Prog. Phys. 60, 151 (1997).
- [29] C.M. Will, Phys. Rep. 113, 345 (1984); T. Damour, to appear in Nucl. Phys. B (Proc. Suppl.) 1999; T. Damour, Eur. Phys. J. C3, 113 (1998); T. Damour, in Les Arcs 1990, Proceedings, "New and exotic phenomena '90", 285 (1990); R.D. Reasenberg *et al.*, ApJ 234, L219 (1979).
- [30] J. Ellis *et al.*, Phys. Lett. B 134, 429 (1984); E. Witten, Phys. Lett. B 155, 151 (1985); H. Nishino, E. Sezgin, Phys. Lett. B 144, 187 (1984); A. Masiero, M. Pietroni, F. Rosati, Phys.Rev. D61 023504 (2000).
- [31] W. Hu, U. Seljak, M. White, M. Zaldarriaga, Phys. Rev. D 57, 3290 (1998).